

Classifying Urban Rainfall Extremes Using Weather Radar Data: An Application to the Greater New York Area

ALI HAMIDI AND NARESH DEVINENI

Department of Civil Engineering, City College of the City University of New York, and NOAA/Cooperative Remote Sensing Science and Technology Center, and Center for Water Resources and Environmental Research, New York, New York

JAMES F. BOOTH

NOAA/Cooperative Remote Sensing Science and Technology Center, and Department of Earth and Atmospheric Science, City College of the City University of New York, New York, New York

AMANA HOSTEN

Department of Earth and Atmospheric Science, City College of the City University of New York, New York, New York

RALPH R. FERRARO

Satellite Climate Studies Branch, NOAA/NESDIS/STAR/CoRP, and Cooperative Institute for Climate and Satellites, Earth System Science Interdisciplinary Center, University of Maryland, College Park, College Park, Maryland


REZA KHANBILVARDI

Department of Civil Engineering, City College of the City University of New York, and NOAA/Cooperative Remote Sensing Science and Technology Center, New York, New York

(Manuscript received 8 August 2016, in final form 3 November 2016)

ABSTRACT

Extreme rainfall events, specifically in urban areas, have dramatic impacts on society and can lead to loss of life and property. Despite these hazards, little is known about the city-scale variability of heavy rainfall events. In the current study, gridded stage IV radar data from 2002 to 2015 are employed to investigate the clustering and the spatial variability of simultaneous rainfall exceedances in the greater New York area. Multivariate clustering based on partitioning around medoids is applied to the extreme rainfall events' average intensity and areal extent for the 1- and 24-h accumulated rainfall during winter (December–February) and summer (June–August) seasons. The atmospheric teleconnections of the daily extreme event for winter and summer are investigated using compositing of ERA-Interim. For both 1- and 24-h durations, the winter season extreme rainfall events have larger areal extent than the summer season extreme rainfall events. Winter extreme events are associated with deep and organized circulation patterns that lead to more areal extent, and the summer events are associated with localized frontal systems that lead to smaller areal extents. The average intensities of the 1-h extreme rainfall events in summer are much higher than the average intensities of the 1-h extreme rainfall events in winter. A clear spatial demarcation exists within the five boroughs in New York City for winter extreme events. Resultant georeferenced cluster maps can be extremely useful in risk analysis and green infrastructures planning as well as sewer systems' management at the city scale.

 Denotes content that is immediately available upon publication as open access.

Corresponding author e-mail: Ali Hamidi, ahamidi@ccny.cuny.edu

DOI: 10.1175/JHM-D-16-0193.1

© 2017 American Meteorological Society. For information regarding reuse of this content and general copyright information, consult the [AMS Copyright Policy](http://www.ametsoc.org/PUBSReuseLicenses) (www.ametsoc.org/PUBSReuseLicenses).

1. Introduction

Urban hydrologic engineering relies on the estimation of design storms for specific durations and return periods. These design storms are based on historical precipitation records for the region of interest.

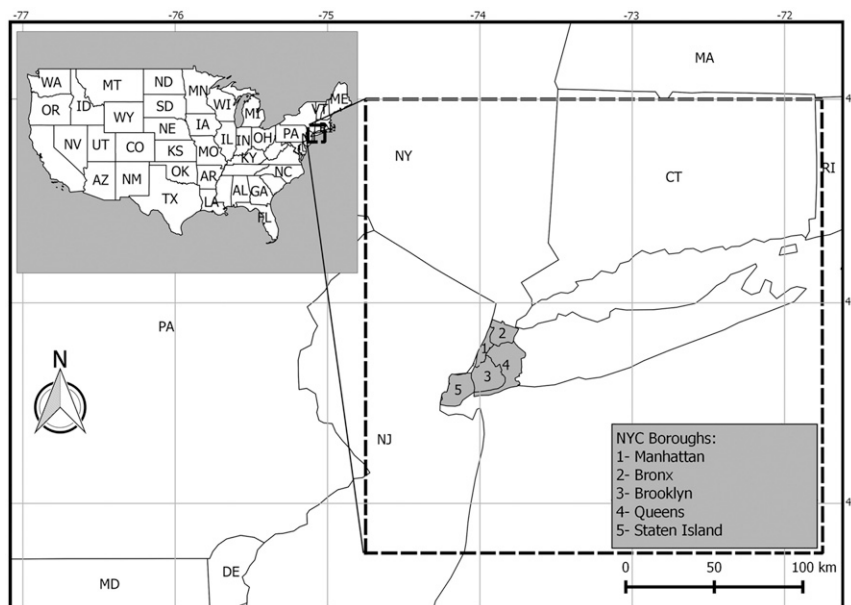


FIG. 1. Study area: GNY and the five boroughs of NYC.

Intensity–duration–frequency (IDF) curves are developed for precipitation and applied to the design of drainage system elements such as sewers, culverts, or control elements such as detention basins (Chow et al. 1988; Kothiyari and Grade 1992; Madsen et al. 2009; Simonovic and Peck 2009). Under the IDF curve approach, typically a single curve interpolated from rain gauges in the area is applied to a catchment (Hershfield 1963). The extreme events are assumed to be independent in time, and the design estimates for each location are computed separately without a spatial dependence structure. However, the spatial variability of rainfall, especially for smaller catchments and shorter durations, is often identified as the primary source of error in investigations of rainfall–runoff processes and hydrological modeling (O’Loughlin et al. 1996; Syed et al. 2003). This issue is particularly important for a dense urban area like New York City (NYC), which operates on combined sewer systems, that is, the rainwater and street runoff along with the sanitary and industrial wastewater are collected in the same sewer and conveyed to treatment plants (NYCDEP 2013).

Much of the storm water flows over impervious surfaces into catch basins in the streets and to sewers. Storm water can pose significant challenges to cities in the form of flooding and combined sewer overflows. The combined sewer overflows and storm discharges vary spatially because of the spatial variations in rainfall and can hence influence the quality of the water bodies to support recreational uses in waterways and nearby beaches. Scenarios that properly address the associated spatial

patterns of rainfall can help improve the operation of these systems and the assessment of system performance, especially as drainage network modifications are considered. Rainfall observations used to develop such scenarios are currently limited spatially by the relatively sparse distribution of rain gauges. With advances in weather radar technologies, a very high-resolution spatial dataset for precipitation is available for most of the United States. A big difference between rain gauges and radar is the punctual-to-areal information, that is, radars are providing gridded spatially distributed rainfall products. These spatial fields can provide a basis for properly understanding the clustering and distributional properties of rainfall intensity, timing, and areal extent. These data can be used for developing stochastic scenarios to evaluate the critical links in an urban hydrologic network and consequently improving the design parameters and operations of these systems, including the component drainage elements and storm water control elements. They can also be used to perform assessments on system vulnerability to local and widespread flooding.

In this paper, we explore the spatial variability of two significant attributes of extreme rainfall events over the greater New York (GNY) area (Fig. 1): the simultaneous areal extent, that is, the grids that have rainfall exceeding a threshold at the same time, and their average intensity by applying the partitioning around medoids (PAM) clustering algorithm (Kaufman and Rousseeuw 1990) on radar rainfall data. Since these extreme events impact specific regions and the physical

processes associated with them vary considerably by location and timing, we focus on understanding the spatial manifestation of these event attributes for specified durations and connecting them to synoptic-scale atmospheric precursors (e.g., circulation patterns and their characteristics). While the spatial structure of extreme rainfall has been explored over large areas (e.g., Tetzlaff and Uhlenbrook 2005; Jones and Carvalho 2012; Bernard et al. 2013; Stevenson and Schumacher 2014), research on the spatial structure of extreme events at rainfall time scales that are critical for urban drainage network evaluation has been limited (Berne et al. 2004; Smith et al. 2012; Wright et al. 2014; Zhang et al. 2014). Furthermore, no literature was found that looked at the areas covered by extreme rainfall and their joint dependence with the intensities and time of occurrence for a specific duration at these scales.

For extreme rainfall of a specified duration, we have considered the partial duration series with events that exceed the 90th percentile of all rainfall at a given grid. We have considered 1- and 24-h accumulations to represent the short- and long-duration rainfall events and seasons of December–February (DJF) and June–August (JJA) to represent winter and summer events, and we used the Next Generation Weather Radar (NEXRAD) hourly weather radar data to identify the extreme rainfall partial duration series. The total area associated with simultaneous exceedance of the 90th percentile is then recorded. For each rainfall duration of 1 and 24 h, and for winter and summer seasons, we are interested in exploring whether there are significant spatially organized clusters in the intensity and areal extent (number of grids exceeding a threshold at the same time). We employ the PAM classifying algorithm to assess the congruence in spatial characteristics and to validate them with reported extreme events in the region using the NOAA Storm Events Database (NOAA/NCEI 2016). The causal factors, that is, the storm mechanisms associated with the clusters for different seasons, are explored in brief in this paper using compositing analysis on ERA-Interim data.

The rest of the paper is organized as follows. The NEXRAD data used in the study and the extreme event identification process are described in section 2. The clustering analysis details and results along with the analysis on atmospheric teleconnections are presented in section 3. In section 4, we present the summary and conclusions.

2. Description and processing of radar rainfall data

The NEXRAD system comprises 160 Weather Surveillance Radar-1988 Doppler (WSR-88D) sites installed

throughout the United States and at selected overseas locations (Heiss et al. 1990). Maximum coverage radius of single radar is 250 nautical miles (~460 km). The WSR-88D continuously collects reflectivity, radial velocity, and spectrum-width base data. These three meteorological quantities are used to generate hydrometeorological products, which are subsequently mapped onto the polar stereographic projection called Hydrologic Rainfall Analysis Project (HRAP; Fulton et al. 1998). An integral part of the precipitation determination algorithms is the ability to dynamically apply the appropriate reflectivity factor Z and rainfall rate R relationship [suggested by Marshall and Palmer (1948); Joss and Waldvogel (1970); Woodley et al. (1975)] with respect to the type of precipitation (e.g., convective or stratiform). While single radar records may suffer from a blockage at certain locations (Vivekanandan et al. 1999; Lang et al. 2009) as well as range limitations, multisensor (gauge, radar, and satellite) products minimize these errors (Miller et al. 2010). Multisensor precipitation estimator (MPE) algorithms provide a real-time suite of gridded radar products at different spatial scales and stages (Hudlow 1988; Vasiloff et al. 2007; Kitzmiller et al. 2013). We refer the readers to Nelson et al. (2010) for more details on weather radars.

In this study, the National Centers for Environmental Prediction (NCEP) stage IV radar product [archived in Gridded Binary (GRIB) format; see WMO (2003)] is employed to produce extreme rainfall fields over the GNY region. Stage IV radar data are a mosaic of the regional multisensor precipitation from all 12 National Weather Service (NWS) River Forecast Centers (RFCs), together with calibration and adjustment for different biases using automatic rain gauge measurement and quality-control processes (Lin and Mitchell 2005). However, stage IV data have a bias for big snowfall events, especially in the east since the RFC stations in the eastern United States do not derive the liquid equivalent precipitation for snow (<http://data.eol.ucar.edu>). Owing to this factor, the stage IV data in the northeastern United States are exclusively rainfall data. The data comprise 1121×881 pixels covering the entire continental United States with the spatial resolution of $4 \text{ km} \times 4 \text{ km}$ and a temporal resolution of 1 h. The 1- and 24-h rainfall radar data are provided by NCEP and are available from the Earth Observing Laboratory (EOL) from 2002 to present with a UTC time stamp. While higher-resolution products are also available for urban areas (e.g., NEXRAD Q2 and Q3 are available at $1 \text{ km} \times 1 \text{ km}$ resolution), they are only archived from 2010. In this study, we used 14 years of stage IV data from 2002 to 2015 to give us as much temporal coverage

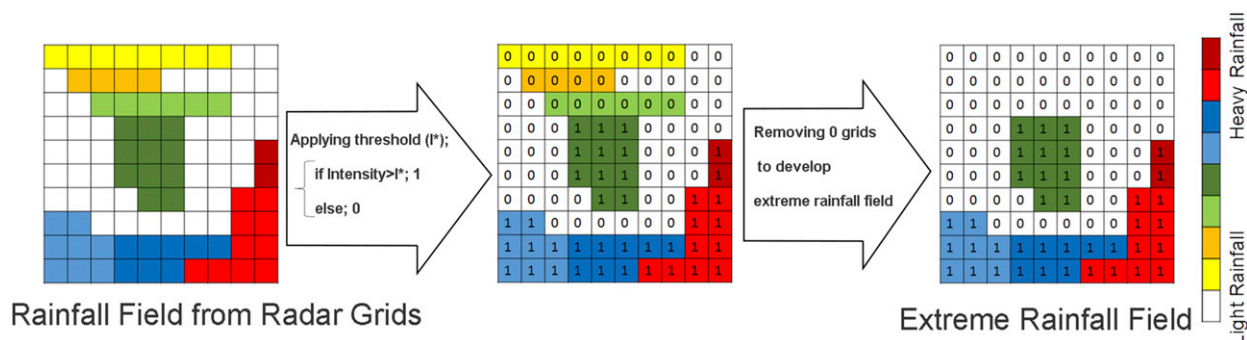


FIG. 2. Schematic procedure of generating extreme rainfall field from radar rainfall data.

as possible. The 24-h data (1200–1200 UTC) are accumulated from the 6-hourly data (Fulton et al. 1998). The probability distribution of rainfall obtained from the radar data conforms well to the probability distribution of the rainfall data obtained from the corresponding rain gauge at John F. Kennedy International Airport, NYC (COOP ID 305803). Zhou (2008) compared radar estimates with rain gauge records in the NYC and Long Island area and showed that at the annual scale, there is little difference between the radar-derived estimates and gauge observations. Allen and DeGaetano (2005) conducted an analysis over the northeastern United States and showed that for extreme precipitation, the areal reduction factors (ARFs) at large spatial scales are similar while independent differences exist between radar ARFs and rain gauge ARFs.

The stage IV data we obtained were further processed as follows to compute the total areal extent and average intensity of the extreme rainfall events.

- 1) The 1-h (accumulated over short duration) and 24-h (accumulated over long duration) rainfall events were identified for the GNY area, which includes 2612 radar grids from the above dataset.
- 2) The 90th percentile R_{90} of the rainfall was determined at each grid box for each of the 1- and 24-h durations.
- 3) We then look through all 122 688 h (5112 days) in the 14-yr record and process the 1 (24)-h rainfall data to identify the rainfall in a grid box that exceeds the estimated R_{90} for that grid box in that hour (day). This process identifies multiple grids across GNY for each hour (day) that meets the criteria of extreme rainfall events. This resulted in a total of 13 258 extreme event hours for the 1-h duration and 1177 extreme event days for the 24-h duration. Among the 13 258 extreme event hours for the 1-h duration, we identify 1401 extreme event hours for the winter season (DJF) and 6316 extreme event hours for the summer season (JJA). Similarly, among the 1177

event days for the 24-h duration, we identify 170 extreme event days for DJF and 487 extreme event days for JJA. Figure 2 schematically indicates an extreme event's field development applying an arbitrary threshold.

- 4) For each rainfall duration of 1 and 24 h, the total area A_i , for the i th event that exceeds the R_{90} , and the corresponding average intensity I_i was recorded. The clustering in the distribution of A_i and I_i for the winter extreme events (DJF) and summer extreme events (JJA) are then investigated using the PAM approach. We chose winter (DJF) to represent the rainfall associated with extratropical cyclones and nor'easters and summer (JJA) to represent rainfall associated with convective storms and hurricanes. Both these seasons are considered important for hazard management in NYC (<http://www.nyc.gov/html/oem/html/hazards/storms.shtml>).

3. Classification of extreme rainfall events' areal extent and intensity

a. PAM clustering analysis

Clustering analysis provides an objective way to classify extreme events into subcategories depending on the multivariate dependence between the variables. The classification can then be linked to the geographic locations to understand the spatial contiguity of the events. A variety of methods for classifying vector data are available. We use the PAM algorithm proposed by Kaufman and Rousseeuw (1990) with a vector of two attributes (A_i and I_i) per event. This classification is very similar to the k -means approach (MacQueen 1967), which partitions the data into k clusters by maximizing the variance across clusters and minimizing the total distance within the cluster. However, the k -means approach represents each cluster center by its mean and does best at identifying the Gaussian mixture data distribution (Bernard et al. 2013), while the PAM

Events:

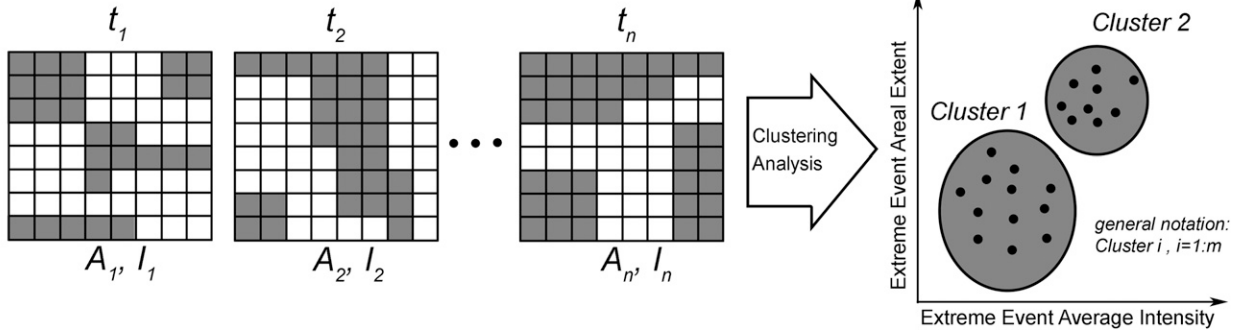


FIG. 3. Attribute vector preparation and clustering approach; for each event, corresponding area, and average intensity are developed as input variables of clustering analysis.

algorithm looks for representative objects, medoids, and minimizes the sum of dissimilarities between the points in the cluster and the medoids. Therefore, the distribution of attribute vector remains unchanged, and no smoothing is performed within PAM. The optimal number of clusters is determined by the maximum mean and minimum number of negative silhouette values. A silhouette is a measure of how cohesive each cluster is and how well the clusters are separated. For n total points in the clusters, a silhouette S_n is defined as

$$S_n = \frac{b_n - a_n}{\max(b_n, a_n)}, \tag{1}$$

where a_n is the average distance from the n th point to the other points within the cluster to which n belongs and b_n is the average distance between the n th point to points in another cluster (Rousseeuw 1987; Kaufman and Rousseeuw 1990). Values of the silhouette range from -1 to $+1$. Clusters with high mean silhouette values are cohesive, and negative silhouette values are possible misclassifications. Hong et al. (2004) and Behrangi et al. (2009, 2010) have employed similar classification approaches for Precipitation Estimation from Remotely Sensed Information Using Artificial Neural Networks–Cloud Classification System to derive finescale rain rates. Figure 3 presents the schematic of the approach used to identify the clusters. For each of the 2612 radar grids in the GNY area, we assign the probability of falling within a cluster as follows:

$$P(C_{ij}) = \frac{n_{ij}}{N_j}, \tag{2}$$

where $P(C_{ij})$ represents the probability of assigning cluster i to grid j , n_{ij} is the number of events of grid j that are in cluster i , and N_j is the number of events of grid j . Accordingly, if all the events (none of the events) of a

grid are grouped in a particular cluster i , then the probability of assigning cluster i to the grid is 1 (0). This way, we essentially understand the properties of a grid regarding their likelihood of experiencing either high-intensity, large-areal-extent events or otherwise.

b. Clustering results

Figure 4 presents the mean silhouette values as a function of the number of clusters. We find the mean silhouette values to be optimal at two clusters for both the 1- and 24-h durations for the winter and summer data. The optimal silhouette values are reported in Table 1. To ensure that the separation in clusters is statistically significant, we performed detailed non-parametric hypothesis tests (Hamill 1999) on both intensity and areal extent by testing the null hypothesis that the means of the clusters are equal. The clusters have different sample sizes (see Table 1). With random variable X denoting cluster 1 and Y denoting cluster 2, the null hypothesis H_0 and the alternate hypothesis H_A for the test are defined as

$$H_0: \bar{X} - \bar{Y} = 0 \quad \text{and} \tag{3}$$

$$H_A: \bar{X} - \bar{Y} \neq 0, \tag{4}$$

where \bar{X} and \bar{Y} denote the means. The distribution of the null hypothesis ($\bar{X}^* - \bar{Y}^*$) is constructed by independently drawing samples (with replacement) from clusters X and Y based on the bootstrap resampling approach (Efron 1979; Efron and Tibshirani 1993). The central idea behind this is to sample with replacement from a pool of data using the underlying distribution that generated the data to guide the sampling process. In other words, the sampling characteristics of a statistic of interest can be simulated by repeatedly treating a single available batch of data in a way that mimics the process of sampling from the parent population. We prefer the nonparametric

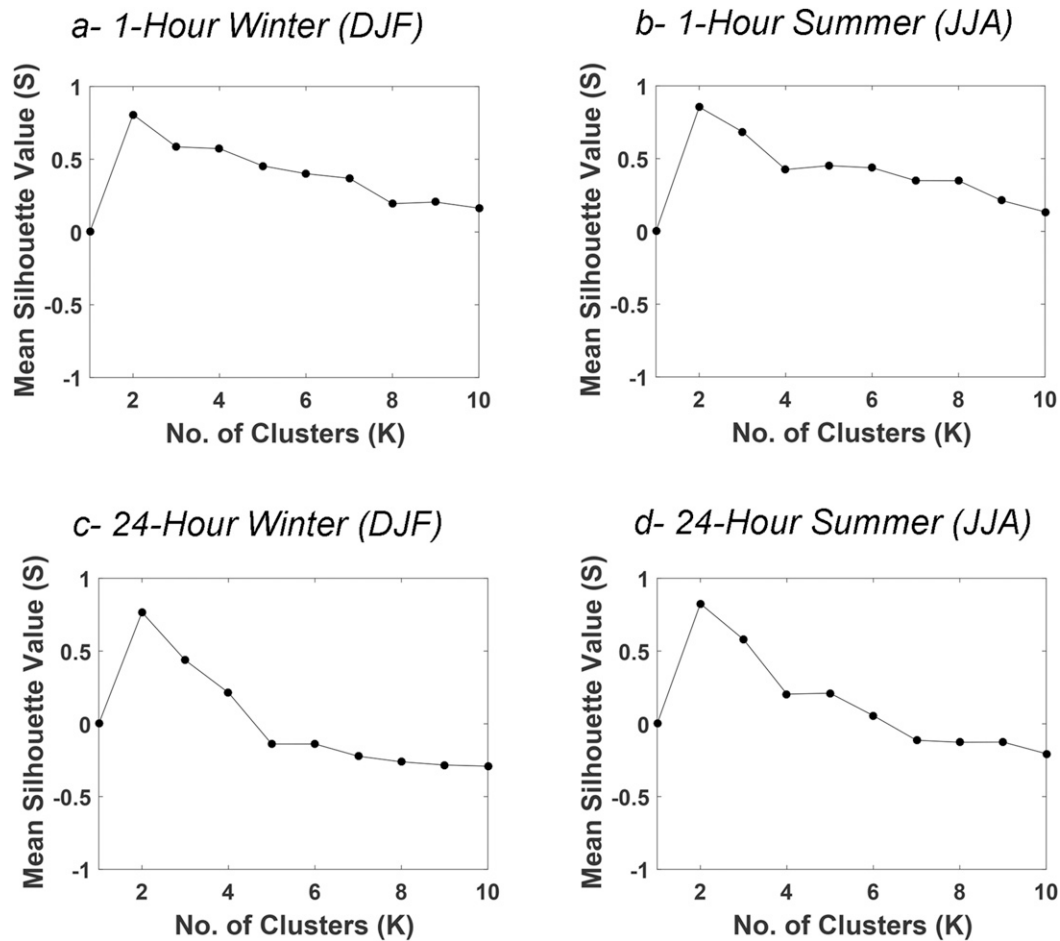


FIG. 4. Mean silhouette coefficient from the clustering analysis; $K = 2$ is the optimum.

approach to the traditional parametric hypothesis tests, as it has the flexibility of treating unequal sample sizes easily and does not need any assumptions on the underlying data distribution. A total of 10 000 estimates of \bar{X}^* and \bar{Y}^* are obtained to develop the null distribution for each test. The percentiles at which the observed test statistic has fallen in the constructed null distribution are computed. For a one-sided hypothesis test, if the percentile of the observed test statistic

($\bar{X} - \bar{Y}$) is between 0.90 and 1, then the mean of cluster Y is lower than the cluster X at a 90% statistical significance interval. Alternately, if the observed test statistic is between 0 and 0.1, then cluster X is significantly lower than cluster Y at the 90% confidence interval. Results from the hypothesis test, the percentile of the observed test statistics on the constructed null distribution, are provided in Table 1, and we identify statistically significant separation in clusters. Cluster 1

TABLE 1. Silhouette values and hypotheses test results from the PAM clustering analysis ($K = 2$) for different rainfall durations.

Timing	Sample size		Silhouette coef	p value (intensity)	p value (areal extent)
	Cluster 1	Cluster 2			
1-h rainfall duration					
DJF	1277	124	0.8	<0.1	<0.1
JJA	4922	1394	0.85	<0.1	<0.1
24-h rainfall duration					
DJF	146	24	0.8	<0.1	<0.1
JJA	451	36	0.82	<0.1	<0.1

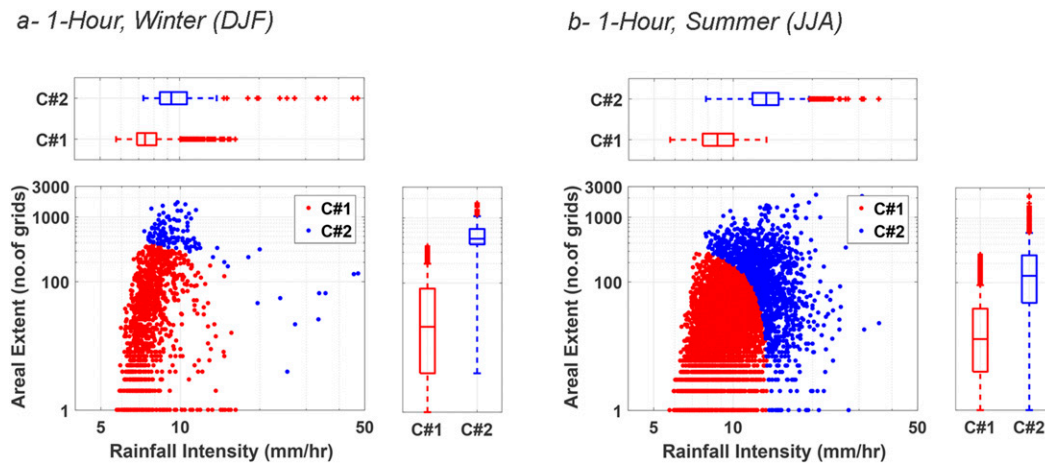


FIG. 5. Results of clustering analysis for the 1-h extreme rainfall data for (a) DJF and (b) JJA. Red and blue colors represent clusters 1 and 2, respectively.

is significantly lower than cluster 2 at the 90% significance level.

1) RESULTS FOR 1-H EVENTS

The outputs of average intensity and areal extent for the 1-h events are presented in Fig. 5, with the scatter-plots showing the joint distribution and the box plots showing the marginal distributions. In each of the winter (DJF) and summer (JJA) seasons, cluster 1 (in red) corresponds to events with low average intensity and small areal extent and cluster 2 (in blue) corresponds to events with high average intensity and large areal extent. From Fig. 5, we observe that for the short duration (1 h), the summer events have higher average rainfall intensities than the winter events. From Fig. 5a, we can observe that the median average intensity of the 1277 winter events in cluster 1 is 7.5 mm h^{-1} . The median areal extent of these events is 20 grids ($\sim 320 \text{ km}^2$). The median average intensity of the 124 winter events in cluster 2 is 9.5 mm h^{-1} . The median areal extent of these events is 500 grids ($\sim 8000 \text{ km}^2$). Similarly, from Fig. 5b, we can observe that the median average intensity of the 4922 summer events in cluster 1 is 8.5 mm h^{-1} and the median areal extent is 15 grids ($\sim 240 \text{ km}^2$). The median average intensity of the 1324 summer events in cluster 2 is 15 mm h^{-1} and the median areal extent is 150 grids ($\sim 2400 \text{ km}^2$).

Figure 6 presents the spatial distribution (georeferencing) of the probability of assigning cluster 2 for the five boroughs in NYC for the 1-h events. As described earlier, we compute the probability of assigning cluster 2 as the number of events of grid j that are in cluster 2 divided by N_j , the number of events of grid j . Blue color in the map indicates that the probability of assigning cluster 2 to the grid is close to 1 in that season. This

implies that most of the events of the grid are grouped in cluster 2 (high intensity and large areal extent), an indication that this grid has a higher likelihood of experiencing extreme rainfall events with high intensity and large areal extent in that season. On the other hand, a red color indicates that the probability of assigning cluster 2 is close to 0, implying that most of the events of the grids are grouped in cluster 1, indicating a lower likelihood of experiencing high-intensity, large-areal-extent extreme events. We can see a clear west-to-east gradient in the spatial distribution of cluster 2 for the 1-h winter extreme events (Fig. 6a), indicating that the grids west of NYC are associated with low intensity and small areal extent, while the grids east of NYC are associated with high intensity and large areal extent for short-duration winter events. Figure 6c, which shows the box plots of the spatial distribution of the probability of cluster 2, provides a closer look at the five NYC boroughs (also see Fig. 1) for the winter events. We see that the borough of Queens (fourth box from the left) has increased likelihood of high-intensity and large-areal-extent short-duration extreme events during winter, compared to the other boroughs. We also observe that, while Manhattan, Bronx, Brooklyn, and Queens have a probability greater than 0.5, the borough of Staten Island has a lower probability for cluster 2 (median is around 0.42), indicating a higher likelihood of events associated with low intensity and small areal extent.

The summer 1-h extreme events (Fig. 6b) are more homogenous, and much of the NYC area experiences high-intensity and large-areal-extent events. Figure 6d (box plots of the spatial distribution of the probability of cluster 2 in the five NYC boroughs for the summer) indicates that all the boroughs have a higher probability of cluster 2. It is important to realize that the median areal

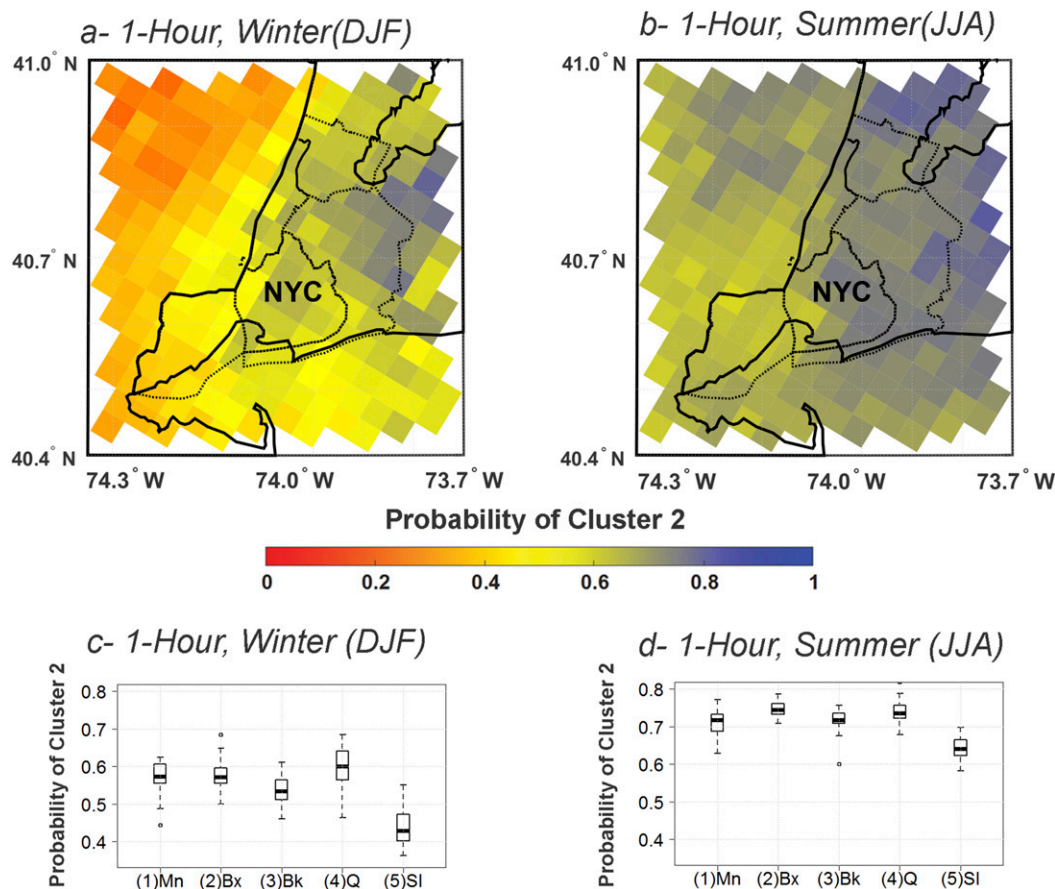


FIG. 6. Spatial distribution of the probability of cluster 2 for the 1-h extreme events over NYC in (a) DJF and (b) JJA. The box plots of the probabilities for the five NYC boroughs are also presented for (c) DJF and (d) JJA.

extent in cluster 2 during winter is larger than the median areal extent in cluster 2 during summer. On the other hand, the average intensity in cluster 2 during winter is much lower than the average intensity in cluster 2 during summer (Fig. 5). This indicates that the winter 1-h extreme events seen in cluster 2 are associated with higher areal extent (a manifestation of synoptic-scale organized storms) compared to the events seen in cluster 2 during summer (a manifestation of more localized convective storms). However, the summer events have greater intensity.

2) RESULTS FOR 24-H EVENTS

The outputs of average intensity and areal extent for the 24-h events are presented in Figs. 7a and 7b. A perusal of the clusters in winter and summer seasons indicates that the average intensities of the events in cluster 2 are similar across seasons with a median average intensity of 1.5 mm h^{-1} . The median average intensity of the winter events in cluster 1 (1.2 mm h^{-1}) is lower than the median average intensity of the summer

events in cluster 1 (1.4 mm h^{-1}). The areal extent of the winter events in cluster 2 (median is around 2000 grids, $\sim 32\,000 \text{ km}^2$) are larger than the areal extent of summer events in cluster 2 (median is around 1200 grids, $\sim 19\,200 \text{ km}^2$), while the areal extents of the events in cluster 1 for winter and summer are comparable.

Figure 8 presents the spatial distribution (georeferencing) and the corresponding box plots of the probability of assigning cluster 2 for the five boroughs in NYC for the 24-h events. We can again notice that for the winter season, the five boroughs exhibit a higher likelihood of having 24-h extreme events with high intensity and large areal extent. Individual differences between boroughs exist, with Queens and the Bronx having the highest probabilities and Staten Island and Brooklyn having lower probabilities. On the other hand, for the summer 24-h extreme events, we find that the probability of falling in cluster 2 is around 0.5 for all the boroughs, making them indistinguishable from random chance. In other words, the 24-h extreme events in these boroughs during summer are mixed between high

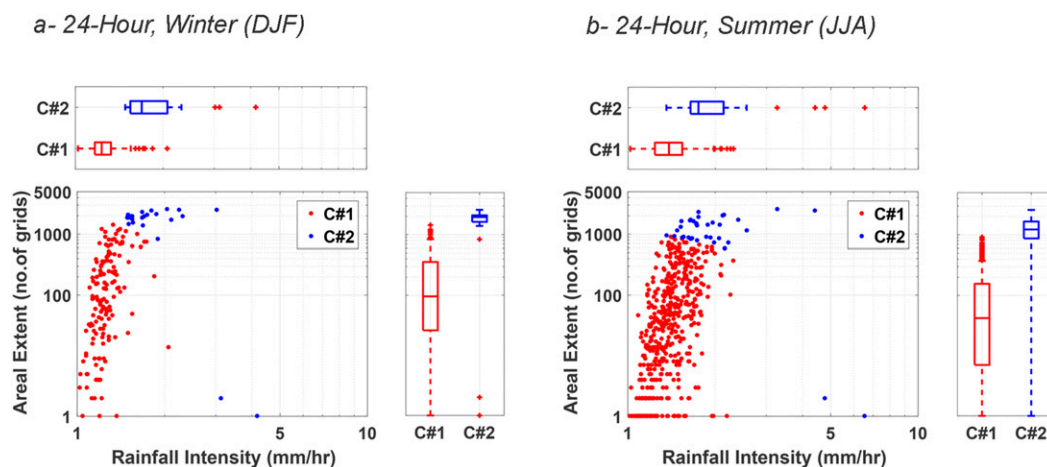


FIG. 7. Results of clustering analysis for the 24-h extreme rainfall data for (a) DJF and (b) JJA. Red and blue colors represent clusters 1 and 2, respectively.

intensity, large areal extent (possible tropical storm and hurricane induced events) and low intensity, small areal extent (possible localized convective storms).

c. Atmospheric teleconnections

In this section, we investigate the meteorological context and the conditions that lead to large areal extent (cluster 2) 24-h extreme events for the GNY area for both winter and summer seasons. Large-areal-extent events may be associated with organized transport of moisture to the region. Hence, we examine the synoptic-scale weather anomalies associated with the events under cluster 2. To do this, we generate composites, using ERA-Interim data (Dee et al. 2011). The composites show the sea level pressure (SLP) and 2-m temperature anomalies. The anomalies are with respect to daily means for 1979–2012, which have been smoothed with a 5-day running mean. SLP provides insights into the circulation patterns and storm strength, while 2-m temperature can help show the importance of advection and/or fronts. Figure 9a shows the composite for the winter season (DJF) based on the 24 events that were classified into cluster 2 under winter. The composite SLP field shows a deep, closed-low circulation typical of extratropical cyclones that generate winter precipitation in the region. The 2-m temperature anomaly shows a dipole of warm and cold anomalies, suggestive of the warm and cold advection generated by the storms. The SLP contours and temperature anomalies are not collocated in the manner observed in individual storms. We interpret this to be a bias introduced by the compositing analysis, partially related to the SLP being full fields and the 2-m temperature being anomalies. The important result in this figure is the identification of the stormlike synoptic pattern expected during winter. The upper-level

circulation moving eastward is reinforced by the surface low and from cold air moving from the south. Moisture is picked up from the ocean surface and the system moves along the coast of the mid-Atlantic and causes precipitation due to horizontal convergence (Miller and Frederick 1969).

We further verified these results using the NOAA Storm Events Database, which contains continental-scale records of the occurrence of storms (from 1950 to present) and other significant weather phenomena having sufficient intensity to cause loss of life, injuries, significant property damage, and disruption to commerce (NOAA/NCEI 2016). From the 24 events in winter classified under cluster 2, we found 14 unique episodes and 28 recorded storm events in the GNY area. An episode is defined as an entire storm system that contains many different types of events. An event is defined as an individual type of storm event, such as thunderstorm, flood, tornado, wind hurricane, etc. An investigation into the episode narratives revealed that many of these episodes were associated with low pressure systems that developed along the Gulf Coast states or in the Tennessee Valley and moved toward the Northeast, causing intense rain or winter weather; a few episodes were associated with slow-moving frontal systems that moved from the Ohio Valley and northeastern Missouri into the GNY region.

For the JJA cases, the heavy precipitation events are most likely caused by frontal storms (Lombardo and Colle 2010), and there is a chance that tropical storms or hurricanes also generated some of the extreme events. To identify the tropical storm events, we adapt a storm association method of Booth et al. (2015), using HURDAT2 (Landsea and Franklin 2013), to identify tropical storm tracks that pass within 1000 km of NYC

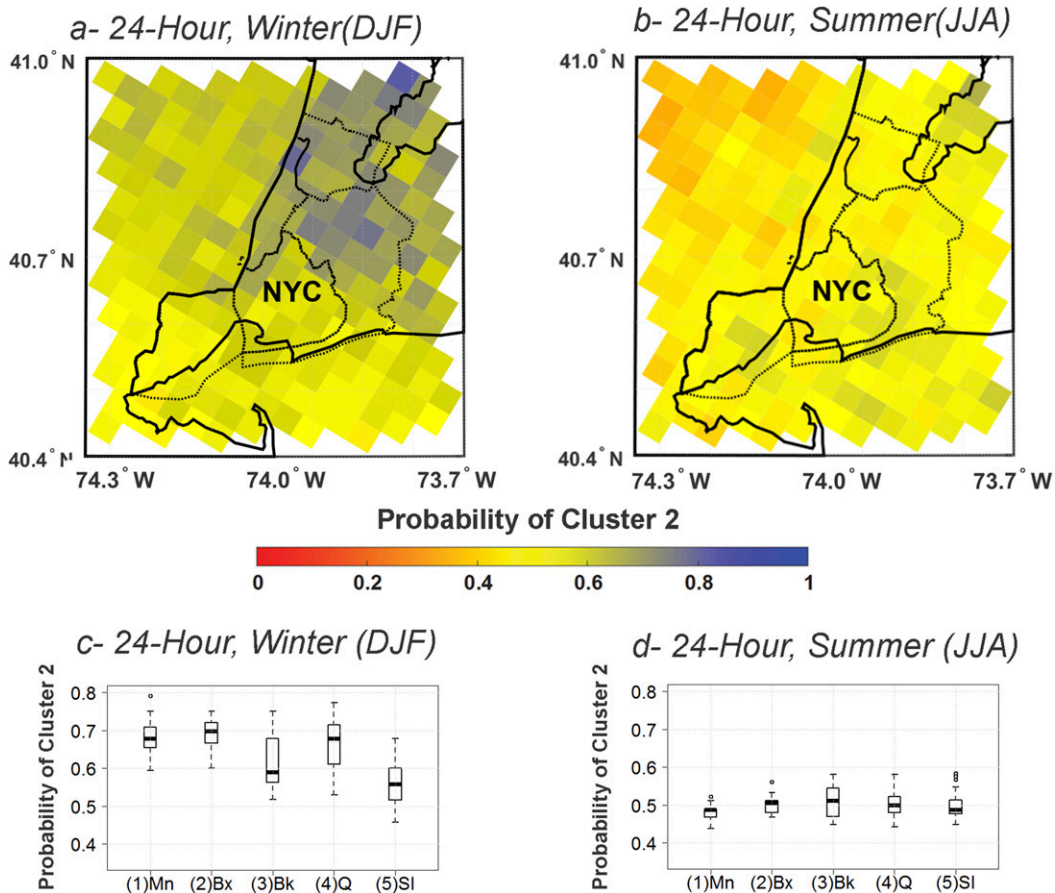


FIG. 8. Spatial distribution of the probability of cluster 2 for the 24-h extreme events over NYC in (a) DJF and (b) JJA. The box plots of the probabilities for the five NYC boroughs are also presented for (c) DJF and (d) JJA.

during the dates of the 36 events in the JJA cluster 2 for 24-h precipitation. We find that four events are either hurricanes or post-tropical storms. Figure 7b shows the composite for the 36 events from JJA, including the four storms with tropical origins (also reported here:

http://www.weather.gov/okx/HistoricFlooding_081314). The SLP contours show a weak closed low, typical of summertime frontal storms in the Northeast (Lombardo and Colle 2010). The 2-m temperature anomaly shows a gradient that is oriented in the southwest-to-northeast

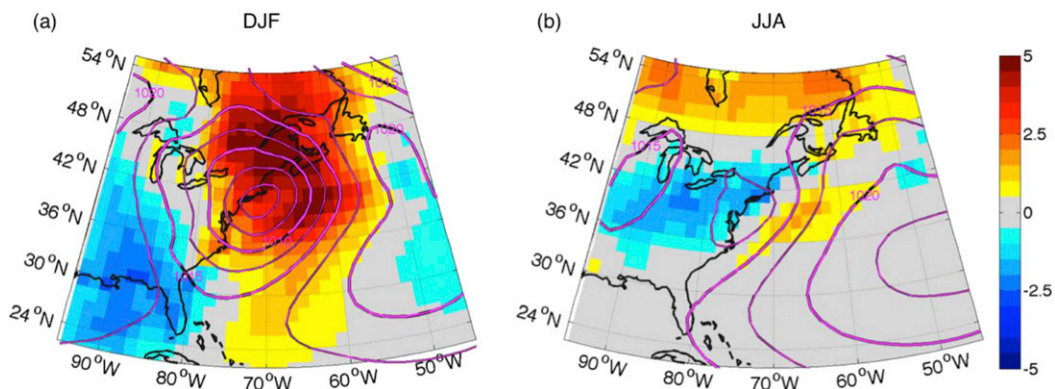


FIG. 9. Composites for cluster 2 events of 24-h extreme rainfall events for (a) DJF and (b) JJA. Contours show the SLP (contour intervals: 2.5 hPa, boldface contours are labeled). Shading shows the 2-m temperature anomaly.

direction, indicative of a cold front, suggesting that these are indeed summertime frontal storms. The gradient in the temperature anomaly field hugs the coastline, and therefore one could assume that the composites are simply capturing a land–sea temperature difference. However, during summer the temperatures of the land and ocean in the climatology are nearly equal, with the land being slightly warmer. Therefore, the anomaly pattern is more likely related to the synoptic structure of summertime frontal storm events. For the summer events, we identified 13 unique episodes and 37 recorded storm events from the NOAA Storm Events Database. Hurricane Irene and Tropical Storm Andrea stand out in these episodes as the major ones; the rest of the episodes are associated with localized thunderstorms that developed along the stationary warm fronts in the region. Taken together, the composites for winter and summer show that, for cluster 2 of the 24-h extreme rainfall events, our analysis of the radar precipitation extremes can be identified with the archetypal storms at the synoptic scale (e.g., [Kunkel et al. 2012](#)).

4. Summary and conclusions

Urban hydrologic systems exist at the interface between natural processes and human impacts. An improved representation of the critical forcing of these systems by meteorological and climatic processes is an essential aspect of predicting the functioning of such systems, especially as drainage network modifications are considered. Moreover, knowledge on extreme events' areal scaling helps in developing improved risk and performance analysis techniques for urban water systems. In this regard we embarked on classifying rainfall extremes based on high-resolution radar rainfall data, exploring the spatial variability at the urban scale, and relating these classifications to synoptic circulation patterns. We first develop spatial fields of extreme rainfall events and compute the average intensity and areal extent of the events for short-duration (1 h) and long-duration (24 h) during winter (DJF) and summer (JJA) seasons. We developed a simple and effective probabilistic classification approach (PAM-based event classification and spatial attribution using probability of occurrence) for these extreme rainfall events and attempted to understand areal coverage by extreme rainfall and its joint dependence with the intensities and time of occurrence. We also investigated the relationships of the classified 24-h events with synoptic circulation patterns and validated them with the storm event database. Following are the main findings:

- 1) For the 1-h duration, the summer extreme events have higher average rainfall intensities than the winter extreme events.
- 2) The areal extent of the high-intensity 1-h extreme rainfall events during winter is larger than the areal extent of the high-intensity 1-h extreme events during summer.
- 3) In NYC, during winter, the borough of Queens has the highest likelihood of experiencing large-areal-extent, high-intensity 1-h extreme events while the borough of Staten Island predominantly experiences low-intensity, small-areal-extent 1-h extreme events.
- 4) For the 24-h duration, the summer extreme events and the winter extreme events have similar intensities.
- 5) The areal extent of the 24-h extreme rainfall events during winter is larger than the areal extent of the 24-h extreme rainfall events during summer.
- 6) In NYC, during summer, all the boroughs have equal probability of experiencing high-intensity, large-areal-extent extreme events and low-intensity, small-areal-extent 24-h extreme events.
- 7) Investigation into the relationships of the 24-h high-intensity classified events reveals that the winter events are associated with deep and organized circulation patterns that lead to more areal extent and the summer events are a manifestation of localized frontal systems, hence leading to smaller areal extents.

Our future work in this direction, building on these findings, will involve using the rainfall extreme fields in conjunction with concurrent synoptic-scale atmospheric circulation patterns to develop spatially distributed stochastic scenarios for urban flood risk estimation and producing coherent flood exceedance maps at the urban scale. We are also focusing on linking the frequency of incidence of these urban precipitation fields to regime-like behaviors seen in large-scale climate precursors (e.g., North Atlantic Oscillation) in order to address some notable gaps in understanding how rainfall processes are manifested in space and time and change with climate.

Acknowledgments. This research was supported by NOAA CREST Cooperative Agreement NA11SEC4810004; the Professional Staff Congress–City University of New York (PSC-CUNY) Award 68670-00 46; the University Transportation Research Center (UTRC) Region 2 award 49198-25 27; the Ralph E. Powe Junior Faculty Award 2015/16 for the second author; and the NOAA Cooperative Institute for Climate and Satellites at the University of Maryland (CICS-MD) Award 76514-05 01. The statements contained within the manuscript are not the opinions of the funding agency or the U.S. government but reflect the

authors' opinions. We thank William Rossow and Michael Grossberg from City College of New York for providing valuable feedback during the inception of this work.

REFERENCES

- Allen, R. J., and A. T. DeGaetano, 2005: Considerations for the use of radar-derived precipitation estimates in determining return intervals for extreme areal precipitation amounts. *J. Hydrol.*, **315**, 203–219, doi:10.1016/j.jhydrol.2005.03.028.
- Behrangi, A., K. Hsu, B. Imam, S. Sorooshian, G. J. Huffman, and R. J. Kuligowski, 2009: PERSIANN-MSA: A Precipitation Estimation Method from Satellite-Based Multispectral Analysis. *J. Hydrometeorol.*, **10**, 1414–1429, doi:10.1175/2009JHM1139.1.
- , —, —, and —, 2010: Daytime precipitation estimation using bispectral cloud classification system. *J. Appl. Meteor. Climatol.*, **49**, 1015–1031, doi:10.1175/2009JAMC2291.1.
- Bernard, E., P. Naveau, M. Vrac, and O. Mestre, 2013: Clustering of maxima: Spatial dependencies among heavy rainfall in France. *J. Climate*, **26**, 7929–7937, doi:10.1175/JCLI-D-12-00836.1.
- Berne, A., G. Delrieu, J. D. Creutin, and C. Obled, 2004: Temporal and spatial resolution of rainfall measurements required for urban hydrology. *J. Hydrol.*, **299**, 166–179, doi:10.1016/S0022-1694(04)00363-4.
- Booth, J. F., H. Reider, D. E. Lee, and Y. Kushnir, 2015: The paths of extratropical cyclones associated with wintertime high wind events in the northeast United States. *J. Appl. Meteor. Climatol.*, **54**, 1871–1885, doi:10.1175/JAMC-D-14-0320.1.
- Chow, V. T., D. R. Maidment, and L. W. Mays, 1988: *Applied Hydrology*. McGraw-Hill, 572 pp.
- Dee, D. P., and Coauthors, 2011: The ERA-Interim reanalysis: Configuration and performance of the data assimilation systems. *Quart. J. Roy. Meteor. Soc.*, **137**, 553–597, doi:10.1002/qj.828.
- Efron, B., 1979: Bootstrap methods: Another look at the jackknife. *Ann. Stat.*, **7**, 1–26, doi:10.1214/aos/1176344552.
- , and R. Tibshirani, 1993: *An Introduction to the Bootstrap*. Chapman and Hall, 456 pp.
- Fulton, R. A., J. P. Breidenbach, D.-J. Seo, D. A. Miller, and T. O'Bannon, 1998: The WSR-88D rainfall algorithm. *Wea. Forecasting*, **13**, 377–395, doi:10.1175/1520-0434(1998)013<0377:TWRA>2.0.CO;2.
- Hamill, T. M., 1999: Hypothesis tests for evaluating numerical precipitation forecasts. *Wea. Forecasting*, **14**, 155–167, doi:10.1175/1520-0434(1999)014<0155:HTFENP>2.0.CO;2.
- Heiss, W. H., D. L. McGrew, and D. Sirmans, 1990: NEXRAD: Next Generation Weather Radar (WSR-88D). *Microwave J.*, **33**, 79–98.
- Hershfield, D. M., 1963: Rainfall frequency atlas of the United States: For durations from 30 minutes to 24 hours and return periods from 1 to 100 years. U.S. Weather Bureau Technical Paper 40, 65 pp. [Available online at http://www.nws.noaa.gov/oh/hdsc/PF_documents/TechnicalPaper_No40.pdf.]
- Hong, Y., K. L. Hsu, S. Sorooshian, and X. G. Gao, 2004: Precipitation Estimation from Remotely Sensed Imagery using an Artificial Neural Network Cloud Classification System. *J. Appl. Meteor.*, **43**, 1834–1852, doi:10.1175/JAM2173.1.
- Hudlow, M. D., 1988: Technological developments in real-time operational hydrologic forecasting in the United States. *J. Hydrol.*, **102**, 69–92, doi:10.1016/0022-1694(88)90092-3.
- Jones, C., and L. M. Carvalho, 2012: Spatial-intensity variations in extreme precipitation in the contiguous United States and the Madden-Julian oscillation. *J. Climate*, **25**, 4898–4913, doi:10.1175/JCLI-D-11-00278.1.
- Joss, J., and A. Waldvogel, 1970: A method to improve the accuracy of radar-measured amounts of precipitation. Preprints, *14th Conf. on Radar Meteorology*, Tucson, AZ, Amer. Meteor. Soc., 237–238.
- Kaufman, L., and P. J. Rousseeuw, 1990: *Finding Groups in Data: An Introduction to Cluster Analysis*. Wiley, 342 pp.
- Kitzmillier, D., D. Miller, R. Fulton, and F. Ding, 2013: Radar and multisensor precipitation estimation techniques in National Weather Service hydrologic operations. *J. Hydrol. Eng.*, **18**, 133–142, doi:10.1061/(ASCE)JHE.1943-5584.0000523.
- Kothiyari, U. C., and R. J. Grade, 1992: Rainfall intensity duration frequency formula for India. *J. Hydraul. Eng.*, **118**, 323–336, doi:10.1061/(ASCE)0733-9429(1992)118:2(323).
- Kunkel, K. E., D. R. Easterling, D. A. R. Kristovich, B. Gleason, L. Stoecker, and R. Smith, 2012: Meteorological causes of the secular variations in observed extreme precipitation events for the conterminous United States. *J. Hydrometeorol.*, **13**, 1131–1141, doi:10.1175/JHM-D-11-0108.1.
- Landsea, C. W., and J. L. Franklin, 2013: Atlantic hurricane database uncertainty and presentation of a new database format. *Mon. Wea. Rev.*, **141**, 3576–3592, doi:10.1175/MWR-D-12-00254.1.
- Lang, T. J., S. W. Nesbitt, and L. D. Carey, 2009: On the correction of partial beam blockage in polarimetric radar data. *J. Atmos. Oceanic Technol.*, **26**, 943–957, doi:10.1175/2008JTECHA1133.1.
- Lin, Y., and K. E. Mitchell, 2005: The NCEP stage II/IV hourly precipitation analyses: Development and applications. *19th Conf. on Hydrology*, San Diego, CA, Amer. Meteor. Soc., 1.2. [Available online at https://ams.confex.com/ams/Annual2005/techprogram/paper_83847.htm.]
- Lombardo, K. A., and B. A. Colle, 2010: The spatial and temporal distribution of organized convective structures over the Northeast and their ambient conditions. *Mon. Wea. Rev.*, **138**, 4456–4474, doi:10.1175/2010MWR3463.1.
- MacQueen, J., 1967: Some methods for classification and analysis of multivariate observations. *Proc. Fifth Berkeley Symp. on Mathematical Statistics and Probability*, Berkeley, CA, University of California, Berkeley, Vol. 1, 281–297.
- Madsen, H., K. Arnbjerg-Nielsen, and P. S. Mikkelsen, 2009: Update of regional intensity–duration–frequency curves in Denmark: Tendency towards increased storm intensities. *Atmos. Res.*, **92**, 343–349, doi:10.1016/j.atmosres.2009.01.013.
- Marshall, J. M., and W. M. K. Palmer, 1948: The distribution of raindrops with size. *J. Appl. Meteor.*, **5**, 165–166, doi:10.1175/1520-0469(1948)005<0165:TDORWS>2.0.CO;2.
- Miller, D. A., D. Kitzmillier, S. Wu, and R. Setzenfand, 2010: Radar precipitation estimates in mountainous regions: Corrections for partial beam blockage and general radar coverage limitations. *24th Int. Conf. on Hydrology*, Atlanta, GA, Amer. Meteor. Soc., 7.2. [Available online at https://ams.confex.com/ams/90annual/techprogram/paper_163622.htm.]
- Miller, J. F., and R. H. Frederick, 1969: The precipitation regime of Long Island, New York. Geological Survey Professional Paper 627-A, 21 pp. [Available online at <https://pubs.usgs.gov/pp/627a/report.pdf>.]
- Nelson, B. R., D. J. Seo, and D. Kim, 2010: Multisensor precipitation reanalysis. *J. Hydrometeorol.*, **11**, 666–682, doi:10.1175/2010JHM1210.1.

- NOAA/NCEI, 2016: Storm Events Database. Accessed 22 July 2016. [Available online at <https://www.ncdc.noaa.gov/stormevents/>.]
- NYCDEP, 2013: New York City combined sewer overflow order on consent: Quarterly progress report—First quarter 2013. New York City Department of Environmental Protection, 53 pp. [Available online at http://www.nyc.gov/html/dep/pdf/cso_long_term_control_plan/2013-q1-cso-quarterly-report.pdf.]
- O'Loughlin, G., W. Huber, and B. Chocat, 1996: Rainfall–runoff processes and modelling. *J. Hydraul. Res.*, **34**, 733–751, doi:10.1080/00221689609498447.
- Rousseeuw, P. J., 1987: Silhouettes: A graphical aid to the interpretation and validation of cluster analysis. *J. Comput. Appl. Math.*, **20**, 53–65, doi:10.1016/0377-0427(87)90125-7.
- Simonovic, S. P., and A. Peck, 2009: Updated rainfall intensity duration frequency curves for the City of London under the changing climate. Water Resources Research Rep., Dept. of Civil and Environmental Engineering, University of Western Ontario, 58 pp. [Available online at <http://ir.lib.uwo.ca/cgi/viewcontent.cgi?article=1027&context=wrrr>.]
- Smith, J. A., M. L. Baeck, G. Villarini, C. Welty, A. J. Miller, and W. F. Krajewski, 2012: Analyses of a long-term, high-resolution radar rainfall data set for the Baltimore metropolitan region. *Water Resour. Res.*, **48**, W04504, doi:10.1029/2011WR010641.
- Stevenson, S. N., and R. S. Schumacher, 2014: A 10-year survey of extreme rainfall events in the central and eastern United States using gridded multisensor precipitation analyses. *Mon. Wea. Rev.*, **142**, 3147–3162, doi:10.1175/MWR-D-13-00345.1.
- Syed, K. H., D. C. Goodrich, D. E. Myers, and S. Sorooshian, 2003: Spatial characteristics of thunderstorm rainfall fields and their relation to runoff. *J. Hydrol.*, **271**, 1–21, doi:10.1016/S0022-1694(02)00311-6.
- Tetzlaff, D., and S. Uhlenbrook, 2005: Significance of spatial variability in precipitation for process-oriented modelling: Results from two nested catchments using radar and ground station data. *Hydrol. Earth Syst. Sci.*, **9**, 29–41, doi:10.5194/hess-9-29-2005.
- Vasiloff, S., and Coauthors, 2007: Improving QPE and very short term QPF: An initiative for a community-wide integrated approach. *Bull. Amer. Meteor. Soc.*, **88**, 1899–1911, doi:10.1175/BAMS-88-12-1899.
- Vivekanandan, J., D. Yates, and E. Brandes, 1999: The influence of terrain on rainfall estimates from radar reflectivity and specific propagation phase observations. *J. Atmos. Oceanic Technol.*, **16**, 837–845, doi:10.1175/1520-0426(1999)016<0837:TIIOTOR>2.0.CO;2.
- WMO, 2003: Introduction to GRIB edition 1 and GRIB edition 2. WMO Doc., 9 pp. [Available online at https://www.wmo.int/pages/prog/www/WMOCodes/Guides/GRIB/Introduction_GRIB1-GRIB2.pdf.]
- Woodley, W. L., A. R. Olsen, A. Herndon, and V. Wiggert, 1975: Comparison of gauge and radar methods of convective rain measurement. *J. Appl. Meteor.*, **14**, 909–928, doi:10.1175/1520-0450(1975)014<0909:COGARM>2.0.CO;2.
- Wright, D. B., J. A. Smith, and M. L. Baeck, 2014: Flood frequency analyses using radar rainfall fields and stochastic storm transposition. *Water Resour. Res.*, **50**, 1592–1615, doi:10.1002/2013WR014224.
- Zhang, Y., J. A. Smith, L. Luo, Z. Wang, and M. L. Baeck, 2014: Urbanization and rainfall variability in the Beijing metropolitan region. *J. Hydrometeorol.*, **15**, 2219–2235, doi:10.1175/JHM-D-13-0180.1.
- Zhou, L., 2008: Annual precipitation pattern over Long Island based on radar data. M.S. thesis, Stony Brook University, 64 pp. [Available online at <https://dspace.sunyconnect.suny.edu/handle/1951/47631>.]